Development and comparison of bare soil moisture retrieval methods for compact polarimetric data

Bhanu Prakash Mookkuthala Erkaramana, Thomas Jagdhuber, Kalifa Goïta, Ramata Magagi, Anke Fluhrer, Florian Hellwig, Hongquan Wang, G. G. Ponnurangam

Development and Comparison of Bare Soil Moisture Retrieval Methods for Compact Polarimetric Data

Bhanu Prakash Mookkuthala Erkaramana⬡, *Graduate Student Member, IEEE*,
Thomas Jagdhuber⬡, *Senior Member, IEEE*, Kalifa Goïta⬡, Ramata Magagi, Anke Fluhrer⬡, *Member, IEEE*,
Florian Hellwig, Hongquan Wang, and G. G. Ponnurangam⬡

Abstract—Retrieval of soil moisture is crucial for weather and climate change predictions as well as in decision-making for agriculture management practices. Several theoretical, semi-empirical, empirical, and machine learning-based scattering models have been developed for simulating fully polarimetric (FP) synthetic aperture radar (SAR) data. The potential of SAR compact polarimetry (CP) for soil moisture retrieval over bare agriculture fields is still an active area of research. In this study, we develop new CP backscattering models for soil moisture retrieval under bare soil conditions. First, we apply empirical relationships between FP and CP to formulate an empirical CP-advanced integral equation model (AIEM). In addition, we propose two adapted theoretical models CP-AIEM and CP-improved IEM (CP-I^{2}EM) using the direct analytical relationship between FP and CP. We also propose two empirical models CP-Dubois and CP-Oh by recalibrating Dubois and Oh models using CP observations and in situ data. To compare the soil moisture retrieval performance of developed CP-backscattering models with that of a standard machine learning approach, the random forest (RF) technique is utilized. The six adapted and developed algorithms are tested using the C-band CP data of Canada's RADARSAT constellation mission (RCM). In situ soil moisture, roughness, and texture measurements were collected from bare agriculture fields of Lennoxville and Montérégie, Quebec, Canada, for calibration and validation of models. Results show that the RF model provides accurate estimates (error: RMSE = 0.04 m^3/m^3, correlation: r = 0.8 and inversion rate:

(IR) = 100%) while requiring extensive training. CP-Oh and CP-Dubois models perform adequately (RMSE = 0.08 m^3/m^3, r > 0.7 and IR > 60%) having limited applicability range. In the end, CP-AIEM offers the best choice including reasonable accuracy (RMSE = 0.07 m^3/m^3, r = 0.6, and IR = 64%), wider applicability range and transferability without requiring calibration.

Index Terms—Bare soil moisture retrieval, compact polarimetry (CP), dubois and Oh models, integral equation model (IEM), RADARSAT constellation mission (RCM), random forest (RF) model, synthetic aperture radar (SAR).

Bhanu Prakash Mookkuthala Erkaramana, Kalifa Goïta, and Ramata Magagi are with the Center d'applications et de recherches en télédétection (CARTEL), Universitéde Sherbrooke, Sherbrooke, QC J1K 2R1, Canada (e-mail: Bhanu.prakash.m.e@usherbrooke.ca; Kalifa.goita@usherbrooke.ca; ramata.magagi@usherbrooke.ca).

Thomas Jagdhuber, Anke Fluhrer, and Florian Hellwig are with the Microwaves and Radar Institute, German Aerospace Center, 82234 Wessling, Germany, and also with the Institute of Geography, Augsburg University, 86159 Augsburg, Germany (e-mail: Thomas.jagdhuber@dlr.de; anke.fluhrer@dlr.de; florian.hellwig@uni-a.de).

Hongquan Wang is with Lethbridge Research and Development Center, Agriculture and Agri-Food Canada (AAFC), Lethbridge, AB T1J 4B1, Canada (e-mail: hongquan.wang@agr.gc.ca).

G. G. Ponnurangam is with the Climate Technology Division, Vassar Labs, Hyderabad 500081, India (e-mail: ggponnurangam@gmail.com).

Digital Object Identifier 10.1109/TGRS.2026.3666196

I. Introduction

SURFACE soil moisture retrieval from observations of active microwave remote sensing has gained significant attention during the last three decades. Microwave sensitivity to dielectric permittivity enables soil water content estimation from radar backscatter [1]. The retrieval of dielectric permittivity from synthetic aperture radars (SARs) backscatter depends largely on the wavelength, polarization, and incidence angle of the observing system [2], [3]. Since microwaves interact with the structure of soil, decoupling of surface roughness from bare soil backscatter has prime importance [4]. In addition, the dielectric behavior of soil depends on its textural composition [5], [6], [7]. Surface scattering models establish relationships between soil surface (dielectric and geometric) properties and radar backscatter, allowing analysis of soil characteristics [8]. The availability of several airborne and spaceborne SAR systems opens the way to enhance continuous observation. These missions operate in a wide range of wavelengths, such as X-, C-, S-, L-, and P-bands, and polarization modes, such as fully polarimetric (FP), dual polarimetric (DP), and hybrid polarimetric. The latter, alternatively known as compact polarimetry (CP), and its circular transmit linear receive (CTLR) architecture are recently gaining attention [9]. Compared to the quadrature polarimetric (QP) architecture, the CTLR does not require time-interleaved transmission and hence limits the pulse repetition frequency to half while doubling the swath. These advantages support the argument of establishing CP as a potential replacement for QP [10]. This has been previously done in earth and planetary missions such as Radar Imaging Satellite (RISAT-1) and Chandrayaan-1 [11], [12], respectively. More recently, the Canadian Space Agency (CSA) has launched the C-band RADARSAT Constellation Mission (RCM) with CP as one of the operational acquisition modes [13]. The higher swath of CP allows to have acquisitions of high temporal resolution without degrading the spatial resolution. Even though CP was introduced decades ago, significantly
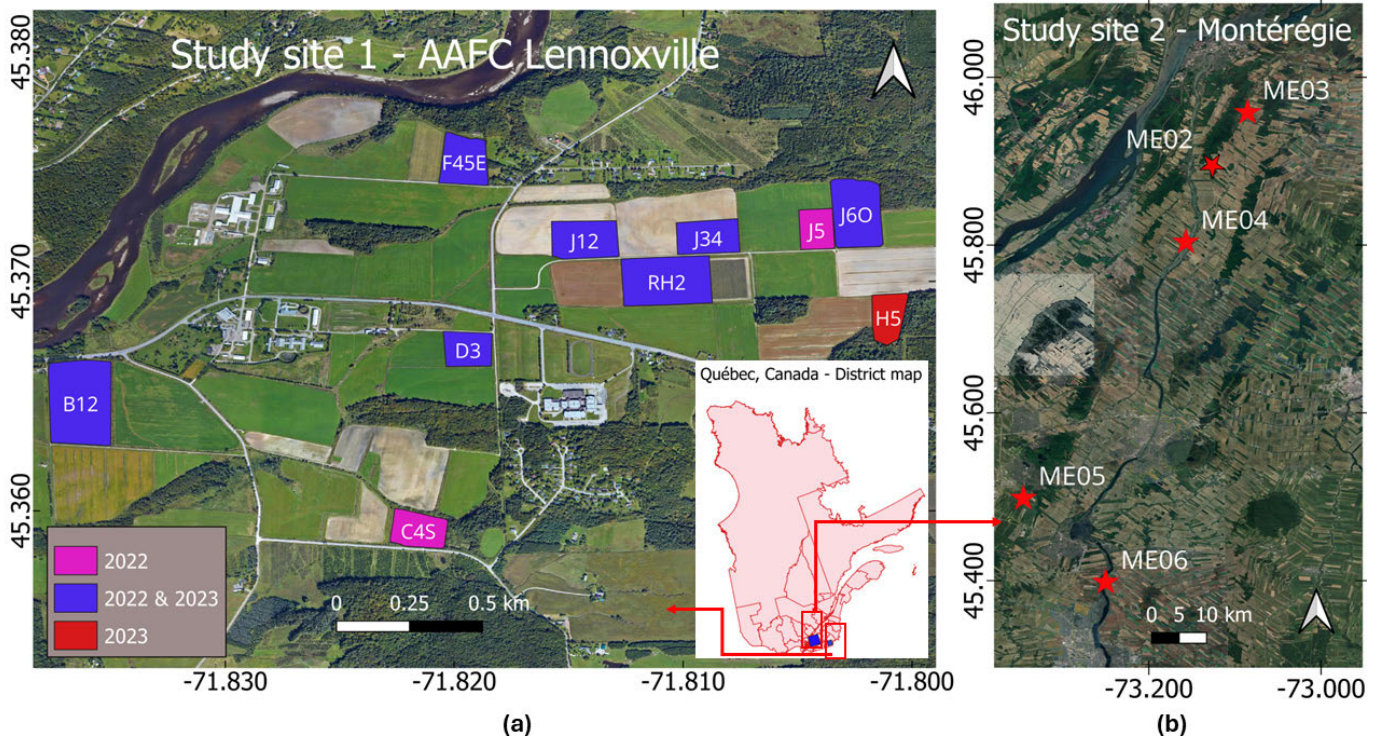
Fig. 1. (a) Study site 1-AAFC Lennoxville displayed on top of the Google satellite layer with fields selected in 2022 (pink), 2023 (red), and both years (violet) are represented. (b) Study site 2-Montérégie region is displayed on top of the Google aerial image with field locations represented by red star symbols. The fields are located far from each other hence the field boundaries are not shown.

fewer soil parameter retrieval algorithms were developed over time compared to FP. This includes soil moisture retrievals based on integral equation model (IEM) and X-Bragg models [14], [15], CP decomposition [16], machine learning [17], and change detection [18]. However, dedicated and generalized surface scattering models, applicable on CP data, have not been extensively established. With this study, we attempt to fill this research gap by developing new CP-based surface backscattering models for bare soil moisture retrievals. We explore different possibilities to develop backscattering models for CP SAR data and perform a quantitative intercomparison that provides guidance to select appropriate backscattering models for soil moisture estimation on bare soils. We propose a total of six theoretical and calibrated empirical backscattering models dedicated to complex CP SAR data.

1) Empirical CP-AIEM.
2) CP-AIEM.
3) CP-I^{2}EM.
4) CP-Dubois model.
5) CP-Oh model.
6) Machine Learning [Random Forest (RF)].

Note that the machine learning approach is used here only for comparison purposes. The essential focus is to develop both physics-based and semi-empirical surface scattering models whose results can be analyzed and interpreted. The proposed models are tested using CP SAR observations of the RCM to assess and compare their applicability for bare soil moisture retrieval. Soil moisture retrieved from these models is validated with in situ measurements collected from bare agriculture soils with different surface roughness and textural composition conditions.

II. STUDY AREA AND DATASET

The selected study sites, in situ measurements and remote sensing data are presented in this section.

A. Study Area

The principal research study site is the Agriculture and Agri-Food Canada (AAFC), Lennoxville (45°21′52″N, 71°48′53″W), Quebec, Canada [Fig. 1(a)]. We have selected ten fields by considering the accessibility, distance from forest and waterbody, and mild geographical slope. The fields selected for the in situ measurements in summer 2022 (pink), 2023 (red), and both years (blue) are shown on top of the Google[1] aerial image. For further analyses regarding the transferability of models, we have included few measurements of another site in the Montérégie region (45°37′52″ N, 72°57′23″ W), Quebec, Canada [Fig. 1(b)].

B. Satellite Data and Preprocessing

C-band (5.405 GHz) right circular CP data of RCM launched by CSA in 2019 are used for this research. The datasets are collected from the Earth observation data management system (EODMS) provided by Natural Resources Canada (NRCan). The three-satellite constellation provides weekly coverage of ScanSAR (30 m spatial resolution) data across the investigated areas at various incidence angles. Table I shows the incidence angle range of each RCM acquisition along with the number of field soil moisture (FSM) measurements made on each day of acquisition. The available RCM data across our sites are in the form of multilook (2 × 2)

[1]Trademarked.

TABLE I

SPECIFICATIONS OF RCM ACQUISITION AND IN SITU SOIL SAMPLING IN
AAFC-LENNOXVILLE AND MONTÉRÉGIE SITES

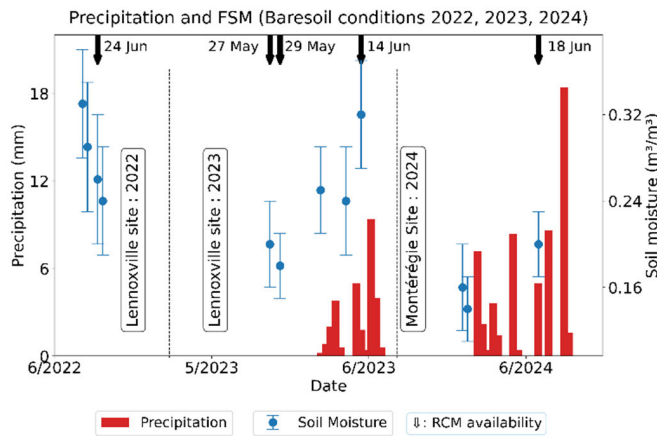| Date of Acquisition	Angle of Incidence (°)	Study site	No. of soil measurements
24-06-2022	17.05-28.90	AAFC-Lennoxville	240
27-05-2023	33.71-42.75	AAFC-Lennoxville	35
29-05-2023	33.70-42.74	AAFC-Lennoxville	118
14-06-2023	33.73-42.74	AAFC-Lennoxville	156
18-06-2024	17.14-28.83	Montérégie	13

Fig. 2. Temporal variation of average in situ FSM (blue dots) and average precipitation (red bars) for the years 2022, 2023 (AAFC-Lennoxville site), and 2024 (Montérégie site) under bare soil conditions. RCM data acquisition dates are represented by black downward arrows and labels.

TABLE II

IN SITU SOIL TEXTURE AND ROUGHNESS MEASUREMENTS TAKEN FROM
AAFC-LENNOXVILLE AND MONTÉRÉGIE SITES

Field / Year	Sand (%) 22-23	Clay (%) 22-23	Silt (%) 22-23	s (cm) 22	s (cm) 23	l (cm) 22	l (cm) 23
AAFC-Lennoxville Site (2022 and 2023)							
B12	28	18	54	1.3	1.7	10.9	8.2
C4S	32	14	54	0.9	-	9.3	-
D3	23	23	54	0.9	2.1	10.7	9.7
F45E	25	20	55	0.9	2.3	9.3	10.7
J12	33	27	40	0.7	2.1	10.1	9.0
J34	24	62	14	2.5	2.3	6.7	10.0
J5	33	19	48	1.2	-	10.6	-
J6O	36	23	41	1.1	2.3	10.1	10.2
RH2	25	36	39	1.5	2.1	12.4	9.0
H5	17	30	53	-	2.2	-	10.6

Montérégie Site (2024)					
	Sand (%)	Clay (%)	Silt (%)	s (cm)	l (cm)
ME2	27	26	47	2.21	9.8
ME3	30	22	48	2.17	8.8
ME4	30	22	48	2.04	9.1
ME5	29	24	47	1.85	7.4
ME6	38	25	37	1.92	8.2

complex (MLC) covariance matrices ([$\mathbf{C_2}$]). The data are then radiometrically calibrated, and speckle filtered (5×5 Boxcar filter). Tandem-X Digital elevation model (DEM) data (30 m spatial resolution) [19] is used for terrain correction and calculation of local incidence angle. Only the pixels with local incidence angles between 20° and 43° are considered to avoid too strong effects of noncircularity [20]. Pixels close to the field boundary and forest area are removed to avoid mixed targets. Only the RCM observations during the crop height less than 10 cm (= 2λ, where λ is the radar signal wavelength) are considered [21] to avoid vegetated soil conditions. The known geographical boundaries of fields were used to spatially subset the RCM data, rather than using any form of image classification strategies, because our focus was primarily on the development of backscattering models.

C. In Situ Data Collection and Preparation

Collection of FSM and soil temperature is done by high-resolution sampling (30×30 m) to match the RCM data resolution using handheld HH2 moisture meters combined with ML3 Theta probe [22]. Each field has a temporary station with rain gauges recording precipitation every 30 min. Surface roughness parameters are measured using a pin-profiler aligned parallel to the look direction of RCM acquisition. The images of pin-profiler are then processed using the QuiP tool to calculate the root-mean square root mean squares (rms) height (s) and the correlation length (l) [23]. Average soil texture in terms of sand (%), silt (%), and clay (%) is extracted from the collected soil samples by laboratory process. Both roughness and texture values are assumed to be invariant within the field and during the entire crop growing season. The measurements are presented in Table II, with 22 and 23 indicating the respective years 2022 and 2023. Temporal variation of average in situ FSM (blue dots) with standard deviation and average precipitation (red bar graph) for 2022, 2023 (Lennoxville) and 2024 (Montérégie) under bare soil conditions is illustrated in Fig. 2.

Precipitation measurements are not available in 2022 for bare soil conditions. The rain events perfectly translate into the spikes in FSM measurements on days 14-06-2023 and 18-06-2024. Good agreement between these measurements advocates the quality of in situ data. The validation samples from wheat fields on days 24-06-2022 and 14-06-2023 are not considered as bare soils, since the crops are already higher than 10 cm.

III. SCATTERING MODELS FOR SOIL MOISTURE RETRIEVALS

Surface scattering models have been developed to investigate the electromagnetic wave emitted or scattered from

random surfaces. They have been widely utilized for estimating roughness and relative permittivity of the surface from radar observation [8]. Each model has validity ranges in terms of wavelength (λ), soil moisture (m_v), dielectric constant (ε), incidence angle (θ), and surface roughness (s and l). Backscattering models may be broadly divided into theoretical, semi-empirical, and empirical ones. Theoretical models can be numerical, which are solved from Maxwell's equations, or analytical, which are simplified from numerical models [4]. These are physics-based models and hence are ideally site-independent. Small perturbation model (SPM), Kirchhoff's Approximation (KA), and IEM are well-known analytical models [21]. SPM is limited to smooth surfaces ($ks < 0.3$ and $kl < 3$), whereas KA provides analytical solutions for scattering from rough surfaces ($kl > 6$ and $2.ks.\cos\theta > \sqrt{10}$) [21], [24]. The normalized surface parameters, ks and kl, are the products of wavenumber (k) with s and l, respectively. Since ks and kl contain wavelength components and are dimensionless, they are more universal than s and l [1]. SPM and KA are extended to IEM by incorporating a complementary tangential term, and the total backscatter is represented as the sum of Kirchhoff's, complementary and cross terms. The scattered fields from the target are represented in terms of tangential fields to calculate co-pol and cross-pol backscatters [1]. An extension of IEM is proposed to reduce the model's gap from SPM and KA at their validity domains [25]. Further, the assumptions used in the Green's function present in the complementary terms are removed and upward and downward scattered field coefficients are added to introduce the Improved IEM (I²EM) [26]. I²EM has better agreement with the SPM for smooth surfaces as compared to the IEM at C-band. However, IEM and I²EM show similar performance when the incidence and scattering angles are the same [8]. Advanced IEM (AIEM) was proposed [27] by rederiving the scattering field coefficients retaining the phase terms of Green's function. This version improves the accuracy of scattering powers as compared to previous versions for rough surfaces [27]. This model was further modified by including the roughness parameters in the calculation of Fresnel reflection coefficients (R_h, R_v) [28]. The results demonstrate considerable improvement in the representation of R_h and R_v for different cases of $\varepsilon, \theta, \gamma, s$ and l. As roughness increases, the differences between AIEM and IEM backscatters increase at every moisture level. Being the extended versions of IEM, our studies show that the resulting FP backscatters from I²EM and AIEM are similar in several cases. Both modifications improve the accuracy of IEM at the cost of an increase in complexity and computation time. In addition to these modifications, calibrated IEM is proposed by building an empirical relationship between l and s [29]. Semi-empirical calibration is also done for the same objective for L-band [30] and then verified and extended to C-band [31]. Recently, several authors have used different versions of IEM for surface parameter retrievals [32], [33], [34].

In contrast to theoretical models, empirical and semi-empirical models are developed to simplify the physical relationship by fitting several parameters [4]. These models are generally site-dependent since the fitting process requires in situ measurements and remote sensing data. The commonly employed semi-empirical models are the Oh [35] and the Dubois models [3], [36]. Inclusion of Dubois and Oh models into this research is to evaluate the potential of empirical backscattering models for soil moisture retrieval from CP data, since they belong to the spectrum of applied backscattering models for soil moisture retrieval. Being empirical models, their constants have limited validity range in terms of incidence angle, roughness, and soil moisture. Despite this limitation, their ease of setting up and inverting for retrieving soil moisture or dielectric permittivity from backscattering coefficient is their main attraction [37]. Unlike the mean-square inversion proposed in IEM-based models, the direct inversion equations can be derived for the Dubois and Oh models. Several studies, including recent ones, suggest that Dubois [38], [39], [40], [41], [42] and Oh [43], [44] models are still actively used for estimating soil moisture, especially when there is a limitation in having accurate in situ roughness data [45], [46]. The Oh model is an empirical calibration of co-pol and cross-pol backscattering coefficients in terms of s, l, and ε [35]. This is modified and reintroduced as a semi-empirical model to relate backscatter and m_v with the assumption that ε varies linearly with R_h and R_v for $0.03 < m_v < 0.35$. The retrieved m_v and roughness reported good agreement with experimental data [47].

In contrast, the Dubois model consists of a pair of empirical equations for the co-pol backscattering coefficient in terms of s, ε, θ, and λ [3]. The equations are straightforward and facilitate unambiguous inversion. However, l and cross-pol backscatter are not considered, and the model is restricted to $\theta > 30°$. In literature, these models are well utilized for soil parameter estimations [45], [46], [48].

In addition to these models, machine and deep learning models such as support vector machine (SVM), random forest (RF), and artificial neural network (ANN) are also widely employed [49], [50], [51]. They are popular because of their capability to build nonlinear relationships between several interdependent variables. Studies show that their accuracies are clearly superior compared to most of the theoretical and empirical methods [52]. However, building such models requires huge training data and hence, are often considered site-dependent and nontransferable [53].

IV. CP FOR SURFACE CHARACTERIZATION

Hybrid/ CP is an SAR architecture that transmits single circular polarization and receives two orthogonal linear polarizations [54]. The most common form of this architecture is CTLR [9], [55]. The possibility of imaging at twice the swath as that of a FP SAR makes it attractive even though it suffers from incomplete backscattering information. However, CP provides more information as compared to a dual-polarimetric SAR [9]. Raney has categorically stated in 2019 and 2021 that CP is sufficient to completely address the target in terms of Stokes parameters [54], [56]. The CP architecture captures all the data received from a resolution cell in the form of two complex scattering coefficients k_{CH} and k_{CV} as shown below [57]

$$\mathbf{K}_C = \begin{bmatrix} k_{CH} \\ k_{CV} \end{bmatrix} = \left(\frac{1}{\sqrt{2}}\right) \begin{bmatrix} S_{HH} & S_{HV} \\ S_{VH} & S_{VV} \end{bmatrix} \begin{bmatrix} 1 \\ \pm j \end{bmatrix}. \tag{1}$$

Here, S_{HH}, S_{HV}, S_{VH}, and S_{VV} are the scattering matrix [S_2] coefficients corresponding to linear transmit-linear receive channels of FP. The signs (–) and (+) denote right and left

circularity. The 2×2 complex covariance matrix ($[\mathbf{C_2}]$) is represented as [57]

$$\mathbf{C}_2 = \begin{bmatrix} c_{11} & c_{12} \\ c_{21} & c_{22} \end{bmatrix} = \mathbf{K}_\mathrm{C} \cdot \mathbf{K}_\mathrm{C}^{*\mathrm{T}}. \tag{2}$$

Here *T denotes the complex matrix conjugate transpose. In our context, we focus on the development of surface scattering models applicable to CP data.

A. Modification of IEM for CP

IEM is a widely used theoretical model which characterizes linear polarized radar backscatters emerging from rough surface [1]. The radar backscatter is represented as a function of target (l, s, ε) and radar imaging (θ and λ) parameters. Transforming these relationships to CTLR is a challenging task. Applying the high-frequency assumption, IEM coefficients can be directly related to co-polarimetric backscattering coefficients [14]. This technique leads to defining a polarimetric scattering mechanism angle (α_s) as a function of IEM coefficients. However, for bare soil, α_s is strongly affected by roughness, and this suggests that the assumptions do not always hold.

B. Empirical CP-AIEM

To overcome the limitations of previous IEM-based models, we need to formulate an algorithm for CP which can consider surface roughness. Therefore, we selected the AIEM algorithm with modified reflection coefficients [28] that are functions of s and l. The single scattering term of the AIEM backscattering coefficients is defined as [28]

$$\sigma_{PQ}^0 = \sigma_{PQ}^k + \sigma_{PQ}^{kc} + \sigma_{PQ}^c$$
$$= \frac{k_1^2}{2} \exp\left[-s^2 \left(k_z^2 + k_{sz}^2\right)\right] \sum_{n=1}^{\infty} \frac{s^{2n}}{n!} \left|I_{PQ}\right|^2 W^{(n)} \tag{3}$$

where $\mathrm{W}^{(n)}$ is the surface roughness spectrum calculated from the autocorrelation function. The three backscattering terms $\left(\sigma_{PQ}^k, \sigma_{PQ}^{kc}, \sigma_{PQ}^c\right)$ denote the Kirchhoff's, cross and complementary field coefficients, P and Q are orthogonal linear polarizations, k_z and k_{sz} are derived from the cosine of incidence and scattering angles, and k_1 denotes the spatial frequency component [28]. Now, the challenge is to transform these equations to the CP domain. Previously, an empirical relationship has been developed from a collection of FP RADARSAT-2 data and simulated CP data under bare soil conditions [15] as follows:

$$\sigma_{CH}^0 = A_1 \cdot \sigma_{HH}^0 + B_1 \tag{4}$$
$$\sigma_{CV}^0 = A_2 \cdot \sigma_{VV}^0 + B_2 \tag{5}$$

where $\sigma_{HH}^0, \sigma_{VV}^0$ are the co-polarization backscattering coefficients for FP and $\sigma_{CH}^0, \sigma_{CV}^0$ are the CTLR backscattering coefficients. The empirical constants A_1, B_1, A_2, and B_2 are 0.85, 0.56, 0.77 and -0.36, respectively, at 30 m spatial resolution [15]. Here, we attempt to use the same empirical relationship to apply these equations on AIEM to develop the empirical CP-AIEM. This modification permits us to incorporate surface roughness into the scattering model for CP backscatter. However, accuracy of this method will depend on the validity of this empirical relationship over the specific study site and radar data.

C. CP-AIEM

To introduce a more robust transformation of theoretical surface scattering models from FP to CP, a physics-based relationship needs to be established. Definition of CP scattering matrix as a function of linear polarizations (1) provides insight into this relationship. We adopt this equation to derive the CP field integrals (I_CH and I_CV) from FP field integrals (I_HH, I_HV, and I_VV). These are functions of Kirchhoff, cross, and complementary field coefficients [28]. This adoption brings the following pair of equations for CP field integrals:

$$I_{CH}^n = \frac{1}{\sqrt{2}} \left(I_{HH}^n - jI_{HV}^n\right) \tag{6}$$
$$I_{CV}^n = \frac{1}{\sqrt{2}} \left(I_{VH}^n - jI_{VV}^n\right). \tag{7}$$

Here, the CP field integrals contain both the co- and cross-polarization field integrals. This is consistent with the definition of CP scattering coefficients in terms of linear polarization (1). We calculate the CP backscattering coefficients from CP field integrals by modifying (3)

$$\sigma_{CH}^0 = \frac{k_1^2}{2} \exp\left[-s^2 \left(k_z^2 + k_{sz}^2\right)\right] \sum_{n=1}^{\infty} \frac{s^{2n}}{n!} \left|I_{CH}^n\right|^2 W^{(n)} \tag{8}$$
$$\sigma_{CV}^0 = \frac{k_1^2}{2} \exp\left[-s^2 \left(k_z^2 + k_{sz}^2\right)\right] \sum_{n=1}^{\infty} \frac{s^{2n}}{n!} \left|I_{CV}^n\right|^2 W^{(n)}. \tag{9}$$

We name this new model CP-AIEM for further analysis. It is important to note that the FP to CP conversion is done before calculating the backscattering coefficient. Utilization of the theoretical relationship between linear and circular polarization assures that these transformations are physically meaningful and lossless.

D. CP-I²EM

Extending the original IEM by removing the assumptions applied to the phase part of Green's function is known as I²EM [8], [26]. No modification has been made in Kirchhoff's term. The complementary field equations of IEM are revised, and a new set of upward and downward propagating field coefficients are introduced. The FP backscattering coefficients are calculated from field integrals with an additional bistatic shadow function (F_S) which is controlled by incidence and scattering angles [26]. Inspired from (6 and 7), we calculate the CP integrals I_CH and I_CV from the I²EM integrals $I_\mathrm{HH}, I_\mathrm{VV}, I_\mathrm{HV}$, and I_VH, leading to the CP backscattering coefficients

$$\sigma_{CH}^0 = F_S \frac{k^2}{2} \exp\left[-s^2 \left(k_z^2 + k_{sz}^2\right)\right] \sum_{n=1}^{\infty} \frac{s^{2n}}{n!} \left|I_{CH}^n\right|^2 W^{(n)} \tag{10}$$
$$\sigma_{CV}^0 = F_S \frac{k^2}{2} \exp\left[-s^2 \left(k_z^2 + k_{sz}^2\right)\right] \sum_{n=1}^{\infty} \frac{s^{2n}}{n!} \left|I_{CV}^n\right|^2 W^{(n)}. \tag{11}$$

We call this new model CP-I²EM in the following.

E. Calibration of CP-Dubois Model

The semi-empirical Dubois model is modified to achieve its CP-calibrated version by replacing $\sigma_{HH}^0, \sigma_{VV}^0$ by $\sigma_{CH}^0, \sigma_{CV}^0$,

TABLE III

CP-Dubois Model Coefficients Calibrated Using the RCM Data and in Situ FSM and Roughness Parameters

	a_1	b_1	c_1	a_2	b_2	c_2
FP	-2.75	0.028	1.4	-2.35	0.046	1.1
CP	-3.32	0.046	0.46	-2.73	0.044	0.30

TABLE IV

CP-Oh Model Coefficients Calibrated Using the RCM Data and in Situ FSM and Roughness Parameters

	g_1	m_1	n_1	g_2	m_2	n_2	g_3	m_3	n_3
FP	0.11	-0.32	1.8	0.095	-1.3	0.9	1	-0.4	1.4
CP	0.14	-0.71	0.5	0.59	-0.52	0.8	1.1	-1.3	0.6

respectively, while keeping the general architecture of the equations as follows:

$$\sigma_{CH}^0 = 10^{a_1} \frac{\cos^{1.5}\theta}{\sin^5\theta} 10^{b_1\varepsilon\tan\theta}(ks\sin\theta)^{c_1}\lambda^{0.7} \quad (12)$$

$$\sigma_{CV}^0 = 10^{a_2} \frac{\cos^3\theta}{\sin^3\theta} 10^{b_2\varepsilon\tan\theta}(ks\sin\theta)^{c_2}\lambda^{0.7}. \quad (13)$$

We call this new model the CP-Dubois model. The calibration data will consist of 50% of the FSM, which corresponds to pixel-level RCM backscattering coefficients ($\theta > 30°$) and field-level ks measurements. The model's six constants a_1, b_1, c_1, a_2, b_2, and c_2 are empirically calibrated by optimizing (12) and (13). The limited memory Broyden–Fletcher–Goldfarb–Shanno algorithm (L-BFGS) is used for the minimization [58]. Table III reports the comparison of original (FP) and modified (CP) model constants.

Constants a_1 and a_2 are slightly increased from the original model. The value of b_1 has increased but b_2 remains approximately the same. It is interesting to note that c_1 and c_2 which are the powers of the roughness term have reduced significantly compared to the original model. This reduces the sensitivity of backscattering coefficients on ks at $\theta > 30°$ and therefore permits wider roughness validity ranges.

F. Calibration of CP-Oh Model

The semi-empirical Oh model for CP backscattering coefficient is adapted by replacing σ_{HH}^0, σ_{VV}^0, σ_{HV}^0 by σ_{CH}^0, σ_{CV}^0, σ_{CX}^0, respectively, to form the set of forward model equations

$$\sigma_{CX}^0 = g_1 * m_v^{0.7} * \cos^{2.2}\theta * \left(1 - e^{m_1(ks)^{n_1}}\right) \quad (14)$$

$$q = g_2 * (0.13 + \sin 1.5\theta)^{1.4} * \left(1 - e^{m_2(ks)^{n_2}}\right) \quad (15)$$

$$p = g_3 * \left(1 - \left(\frac{2\theta}{\pi}\right)^{0.35m_v^{-0.65}}\right) * \left(e^{m_3(ks)^{n_3}}\right) \quad (16)$$

where

$$p = \frac{\sigma_{CH}^0}{\sigma_{CV}^0} \text{ and } q = \frac{\sigma_{CX}^0}{\sigma_{CV}^0}. \quad (17)$$

We name this new model the CP-Oh model. It has nine unknowns (coefficients) as compared to six in the CP-Dubois model and hence requires a greater number of training samples. The calibration data consist of 75% of the measured FSM and field ks to meet the requirement of calibrating the model's coefficients. Even though the validity range of the Oh model is $0.03 < m_v < 0.35$ m³/m³, here we use the complete range of FSM (0.01–0.45 m³/m³). The coefficients g_i, m_i, and n_i are empirically calibrated using the L-BFGS optimization of the set of (14)–(17). The calibration is influenced by incidence angle and hence the calibration constants are different for cases of $\theta < 30°$ and of $\theta > 30°$. The coefficients for $\theta > 30°$ are presented in Table IV to compare with the original Oh

model. It shows that the coefficients g_1, n_2, and g_3 have minor variation from the original model, while the other calibrated parameter values significantly differ from the Oh 2004 model. Parameters m_1, n_1, m_3, and n_3 are smaller and g_2, m_2 are larger compared to the original.

We see from (15) that roughness can be directly calculated from q. Coefficient g_2 is an important parameter in this equation and has the largest variation from the original model.

G. RF Regression Model

RF is used here only for the comparison to the developed theoretical and empirical CP models. It is a popular machine learning model employed as an ensemble decision tree algorithm [17], [59] which uses the concept of boosting and bagging with additional layers of randomness [60]. We randomly split the data into training and testing samples with a 60:40 ratio and select the most important parameters by multiple trials of input combinations. The hyperparameters such as number of trees and leaf size are fixed by optimization using training samples to avoid overfitting. RF regressor is then employed to predict soil moisture.

H. Soil Moisture Inversion

Inversion refers to the estimation of soil moisture from the backscatter, and the approach is different for each model. The inversion equations for theoretical models are complex and not straightforward. There are various parameter optimization techniques, such as look-up-table (LUT) [15], Bayesian inference [61], particle swarm optimization [62], and machine-learning [63]. LUTs are computationally simpler and faster at retrieval time because they avoid iterative optimization and repeated forward modeling [64]. LUTs are easier to implement, and each retrieval corresponds directly to precomputed model simulations. This makes LUTs attractive for large-area, and operational soil moisture retrievals where robustness and speed are critical [61]. In this work, we generate an LUT that consists of backscattering coefficients simulated using each theoretical model (empirical CP-AIEM, CP-AIEM, and CP-I²EM) with different combinations of θ and ε and in situ measurements of ks and kl. Dielectric constant inversion from RCM data is done using the two-parameter inversion by applying the LUT [14], [15] such as

$$\Delta = \sqrt{\left(\sigma_{CH,RCM}^0 - \sigma_{CH,LUT}^0\right)^2 + \left(\sigma_{CV,RCM}^0 - \sigma_{CV,LUT}^0\right)^2}. \quad (18)$$

It is evident from (1) that linear cross-polarization (S_{HV}, S_{VH}) information is not separately available in the CP scattering matrix. However, studies suggest that they are less effective than co-pol channels to represent the dielectric and roughness properties of bare soil [1], [28], [35] due to the dominance of surface scattering over volume scattering. Moreover,

the simulated cross-pol channel backscattering coefficients in these studies are of very low intensity (< -30 dB) in the incidence angle range $20°$–$40°$, which could be quite similar or lower than the nominal noise equivalent sigma zero (~ -25 dB) prescribed for SAR data [65]. Unavailability of a separate cross-pol channel in CP SAR will not add much uncertainty to soil moisture estimations. Thus, we assume that CP backscattering coefficients (σ_{CH}^0 and σ_{CV}^0) are sufficient to characterize the rough soil surface. The σ_{CH}^0 and σ_{CV}^0 are strongly correlated (r ranges from 0.85 to 0.99) with each other and have similar sensitivity to soil moisture under bare soil conditions at different incidence angles and roughness cases. Nevertheless, both CH and CV channels were used in the optimization to minimize the retrieval error. Moreover, both terms were given the same weight in (18). We have established a scatterplot between predicted and measured soil moisture for each theoretical model, with indication of the parameter Δ, which is the difference between the RCM ($\sigma_{CH,RCM}^0$ and $\sigma_{CV,RCM}^0$) and simulated ($\sigma_{CH,LUT}^0$ and $\sigma_{CV,LUT}^0$) backscatters. We found from our analysis that if the value of Δ is large ($\sim > 2$ dB), the retrieved soil moisture is outside of the physical range of FSM (0.01–0.45 m³/m³). We classify these pixels as noninvertible and exclude them from the calculation of RMSE. Even among invertible pixels, retrieval errors can still vary.

There can be multiple local minima occurring in the mean-squared inversion. Having said that, this is widely known and considered when inverting IEM-based scattering models because of the model complexity and hassle of deriving direct inversion equations [14], [62], [63]. The two-parameter inversion has two minimizers that help to constrain the solution space and reduce the ambiguity compared to single-parameter inversion (based on CH or CV backscatters or any other parameter). To avoid the ill-conditioned nature of LUT-based inversion, field surface roughness was provided as an input, thereby reaching a single minimum value. We found that there is always a difference of 0.01–0.3 dB between the first and the second minimums for all the invertible pixels ($\Delta < 2$ dB). This confirms the unambiguity of finding the best match from the LUT corresponding to RCM backscatter.

To ensure reliable validation, we define a spatial inversion rate (IR), which is the ratio of the number of invertible pixels with a threshold RMSE to the total number of validation samples. We selected a reasonable RMSE threshold of 0.05 m³/m³, which corresponds to approximately 10% relative error based on the physical range of FSM indicated previously. This threshold aligns with typical error tolerances in soil moisture retrievals from remote sensing [66]. Dielectric constant is inverted using the CP-Dubois model by the direct inversion in the following equation:

$$\varepsilon_a = 10^{-a_2} \sigma_{CV}^0 \left(\frac{\sin^3 \theta}{\cos^3 \theta} \right) (ks * \sin \theta)^{-c_2} * \lambda^{-0.7} \quad (19)$$

$$\varepsilon = \frac{1}{b_2 * \tan \theta} \log_{10} \varepsilon_a. \quad (20)$$

The CP-Oh model allows inversion of soil moisture directly from RCM backscatters as

$$m_v = \left[\frac{0.35 \log_e \frac{2\theta}{\pi}}{\log_e \left[1 - \frac{p}{g_3} e^{-m_3 (ks)^{n_3}} \right]} \right]^{\left(\frac{1}{0.65} \right)}. \quad (21)$$

Soil moisture estimates of the CP-Dubois and CP-Oh models are also filtered with the same physical range defined above. In the RF model, the soil moisture inversion is done using the regression algorithm itself. Dobson's dielectric mixing model [5] is used to calculate soil moisture from the inverted dielectric constant in all models except CP-Oh and RF models. The mixing model uses the texture constant (β) as an input parameter, which is a function of sand and clay fractions in the soil [5].

V. RESULTS AND DISCUSSION

A. Field Measurements Versus CP Backscatter

In the following, the relationship between the field averages of CP backscattering coefficients (σ_{CH}^0 and σ_{CV}^0) and FSM is studied along with the variation of ks and kl (the figure is not shown here). The in situ data are stratified in terms of the range of local incidence angles of RCM. In general, σ_{CH}^0 and σ_{CV}^0 variations are quite similar for all levels of FSM as well as soil roughness (ks, kl) and incidence angle (θ). Backscatter intensities vary from -10 to -5 dB at low θ and from -18 to -10 dB at high θ. CP backscattering coefficients have negative Pearson's correlations (r = -0.55) with FSM at $\theta < 24°$ and positive correlation (r = 0.85) at $\theta > 36°$. When FSM increases, the backscatter intensity increases from -16 to -10 dB when $\theta > 36°$. In the case of ks, there is a positive correlation (r = 0.75) for $\theta < 24°$ but no specific relationship at $\theta > 36°$. This is because we have more variability in roughness values during the low incidence angle acquisitions. At lower θ, the backscatter has an inverse relationship with kl (r = -0.2). It is evident from the plots that the relationship between CP backscatter and FSM is nonlinear and is affected by other key factors such as θ, ks, and kl. The proposed CP scattering models for rough surfaces will address these multiple and nonlinear relationships.

B. Empirical CP-AIEM, CP-AIEMo, and CP-I²EM

The performance of the IEM-derived models for CP data is presented hereafter. The CP backscattering coefficients are simulated for the different ks, kl, ε, and θ using (3)–(5) for empirical CP-AIEM (red), (6)–(9) for CP-AIEM (blue), and (10) and (11) for CP-I²EM (green) and plotted against RCM backscatter (Fig. 3). Each subplot in Fig. 3 displays variation of σ_{CH}^0 with ε varying from 1 to 25, and three different incidence angles $20°$ (solid line), $30°$ (dashed line), and $40°$ (dotted line) and with a fixed ks and kl combination. In general, σ_{CH}^0 increases as dielectric constant (ε) and vertical roughness (ks) increase and reduces with an increase in kl (smoother horizontal roughness). In almost all cases, the intensity of the σ_{CH}^0 simulated from empirical CP-AIEM is larger than CP-AIEM. For a lower roughness slope (high kl and low ks), both modeled σ_{CH}^0-values are approximately the same. However, as the slope increases (ks increases or kl reduces), there are significant differences in the σ_{CH}^0 intensities between the individual models. When ks is small [Fig. 3(a)–(c)], σ_{CH}^0 simulated from all models converges when decreasing the incidence angle toward $20°$, while it diverges when increasing toward $40°$ incidence. At high ks [Fig. 3(g)–(i)], the difference between the σ_{CH}^0 of different models increases significantly regardless of θ. For variations of kl, the effect is inverse, and this difference decreases regardless of θ. At very high roughness conditions
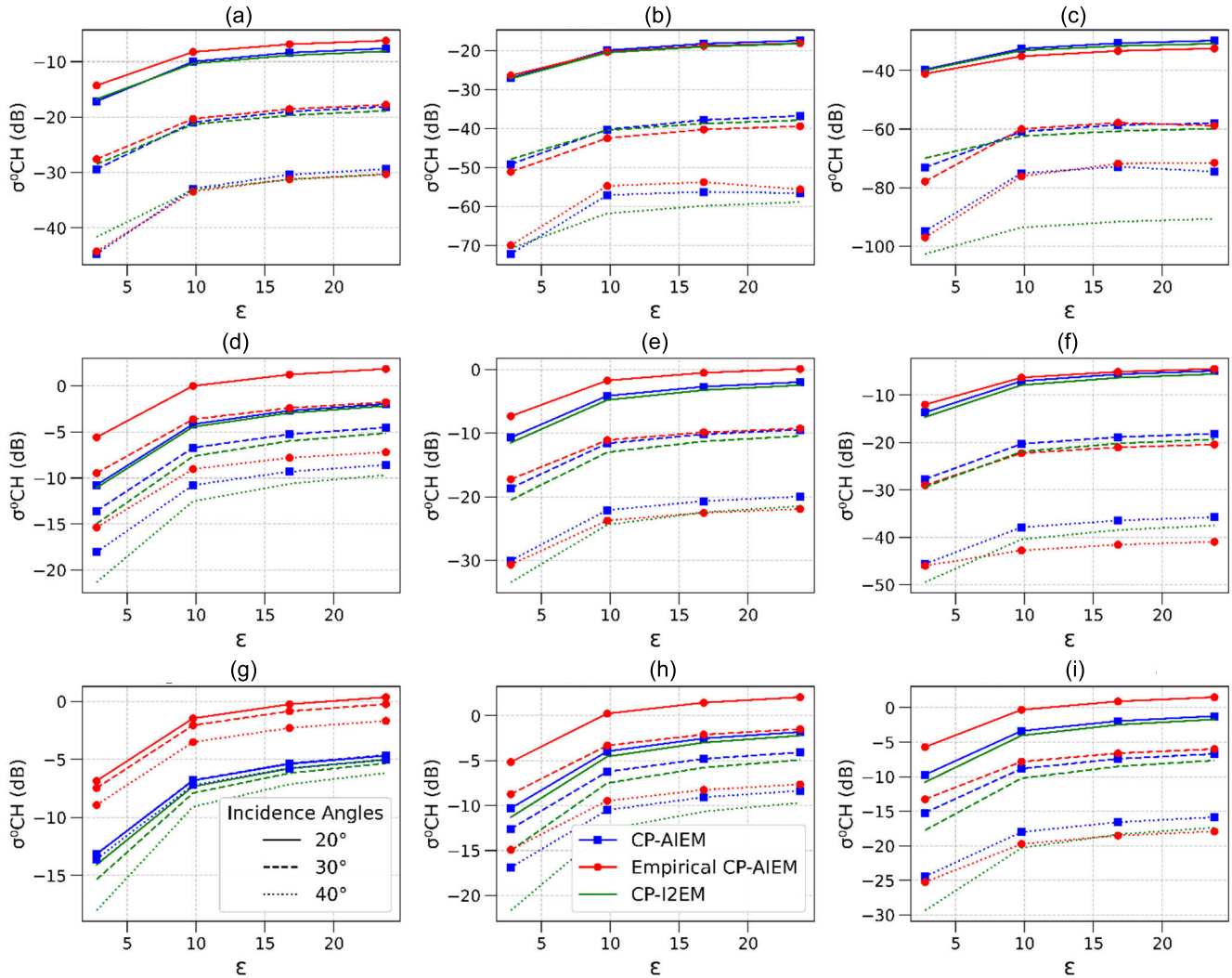
Fig. 3. Comparison between CP-based IEMs: comparison of σ^0_{CH} corresponding to CP-AIEM (blue), empirical CP-AIEM (red), and CP-I²EM (green) simulated using different combinations of ks (0.5, 1.5, 2.5), kl (6, 10, 14), and θ (20°: solid line, 30°: dashed line, 40°: dotted line) with ε varying from 1 to 25. (a) $ks = 0.5$, $kl = 6.0$. (b) $ks = 0.5$, $kl = 10.0$. (c) $ks = 0.5$, $kl = 14.0$. (d) $ks = 1.5$, $kl = 6.0$. (e) $ks = 1.5$, $kl = 10.0$. (f) $ks = 1.5$, $kl = 14.0$. (g) $ks = 2.5$, $kl = 6.0$. (h) $ks = 2.5$, $kl = 10.0$. (i) $ks = 2.5$, $kl = 14.0$.

[Fig. 3(g)], the empirical CP-AIEM backscatter intensity is much higher than CP-AIEM and CP-I²EM. At high roughness conditions, σ^0_{CH} simulated with CP-AIEM are consistently slightly higher than that from CP-I²EM, though they produce very similar results. However, simulated σ^0_{CH} of empirical CP-AIEM is significantly different from the other two. Variation of σ^0_{CV} is overall concurrent with σ^0_{CH} except for the difference in intensity level (the figure is not shown here). It should be noted that this analysis is purely based on forward modeling, and the simulated backscatter of very low intensity (less than -30 dB) is practically impossible to measure in real-world satellite measurements.

Fig. 4 presents the comparison between the modeling of backscatter using theoretical (CP-AIEM, CP-I²EM, and empirical CP-AIEM) and empirical (CP-Dubois and CP-Oh) models with RCM CP backscattering coefficient. The plots are presented by separating the data into three ranges of θ ($\theta < 24°$, $24° < \theta < 36°$, $\theta > 36°$). The relationship between the backscatters is similar in all three models, except for the difference in the simulated backscatter intensity.

A very good correlation with r ≥ 0.8 and p < 0.01 between simulated and RCM backscatters is observed. Simulated CP-AIEM backscatter [Fig. 4(a)] is located closest to the 1:1 line compared to the other two models. Most of the values lie in the ± 2 dB range. In this specific case with the in situ FSM, ks and kl values, CP-I²EM backscatter [Fig. 4(b)] shows a slight overestimation of σ^0_{CV} and underestimation of σ^0_{CH} of around 1 dB when compared to the RCM backscatter. This agrees with the slight difference between CP-AIEM and CP-I²EM simulated backscatters observed in Fig. 3. However, the simulated backscatter of empirical CP-AIEM [Fig. 4(c)] overestimates the backscattering coefficient for rough surface conditions. Some of the RCM backscatter values at mid-incidence angle are not well represented in IEM-based models. In contrast to the general trend in the simulation, a few exceptions are identified. Further analysis on this exception reveals that two small patches deviated from the trend (above and below the trend line) belong to field J12. This is visible in both σ^0_{CV} and σ^0_{CH} plots on a particular date (27-05-2023) with data acquisition at mid-incidence angle ($24° < \theta \leq 36°$).
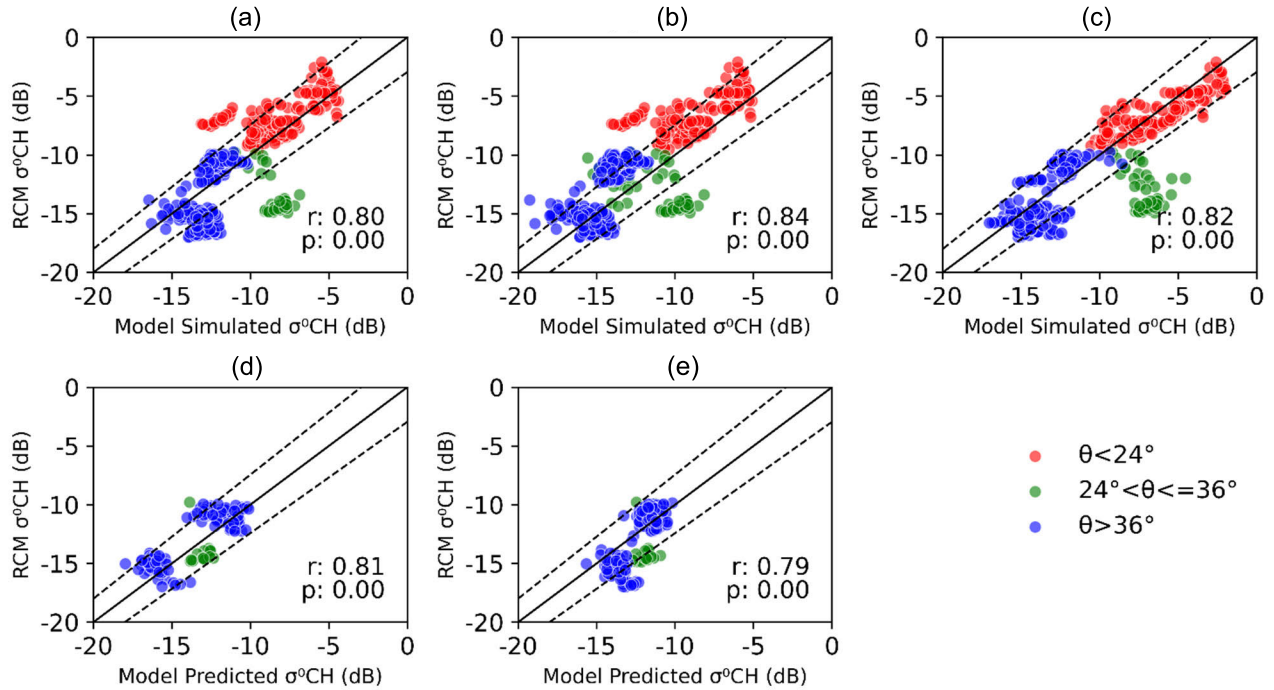
Fig. 4. Correlation between σ_{CH}^0 of RCM and σ_{CH}^0 simulated from in situ measurements using theoretical models (a) CP-AIEM, (b) CP-I^{2}EM, and (c) empirical CP-AIEM and RCM σ_{CH}^0 at all incidence angles. Correlation between RCM σ_{CH}^0 and σ_{CH}^0 predicted by calibrated empirical models (d) CP-Dubois and (e) CP-Oh models and RCM σ_{CH}^0. For empirical models, the green points are for the range $30° < \theta < 36°$.

Also, the patch above the trend line corresponds to the same field but on a different date (24-06-2022). This deviation is present regardless of the FSM value, not observed in any other fields at similar θ values and hence points to ks and kl representing a special case in field roughness. Field J34 is the second exception, which is identified from the σ_{CH}^0 plot with the highest backscattering value. Being the roughest field in 2022 with high ks and low kl, the model is underestimating the backscatter intensity at $\theta < 24°$.

Fig. 4(d) and (e) presents the correlation between backscatter predicted by the CP-Dubois and CP-Oh models after calibration. There are lower number of points involved in the calibration of the CP-Dubois model since we do not use training samples with $\theta < 30°$, respecting the validity range of the original model. The number of calibration and validation samples is 134 and 135, respectively (50% testing-training split). The calibration has an RMSE of 1% and 2%, respectively, for σ_{CV}^0, σ_{CH}^0. There is a good correlation between predicted and RCM backscatter, with r = 0.81 and p-value < 0.01.

Since the CP-Oh model calibration is performed with $\theta > 30°$ and a 75:25 sampling strategy, there are 201 samples available for calibration and 67 samples for validation.

The minimum RMSEs achieved after the optimization are 2%, 2%, and 1% for σ_{CH}^0, σ_{CV}^0, and σ_{CX}^0, respectively. Good correlation (r = 0.79, p < 0.01) between the predicted and RCM backscatters is also observed. However, with the calibration samples of $\theta < 30°$, the model overestimates the backscattering coefficients, and the RMSE increased to 10%. Therefore, we have limited the calibration only to higher incidence angle ranges ($\theta > 30°$).

For comparison with theoretical and empirical models, the RF model is trained using RCM CP parameters, FSM, ks,
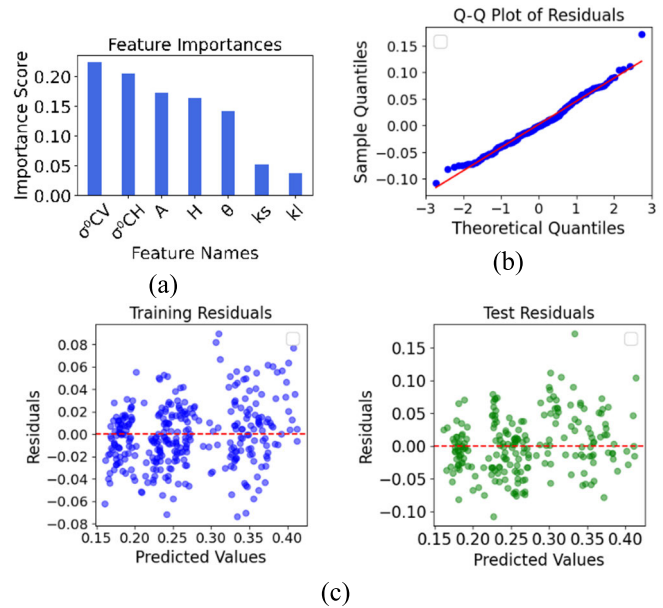

Fig. 5. RF model calibration and validation (a) feature importance analysis among the selected CP parameters with respect to in situ FSM (b) quantile-quantile plot (c) training and testing residuals with predicted FSM.

and kl. The random splitting of testing and training data is done with a 40:60 strategy (175 and 263 samples, respectively). Stratified sampling ensures that the training and testing splits have the same distribution of classes as the original dataset. Unlike empirical or theoretical models, the RF model does not have any limitation on the range of FSM or θ. The correlation study between FSM and different CP parameters allows us to select the most important set of variables for the ML algorithm.
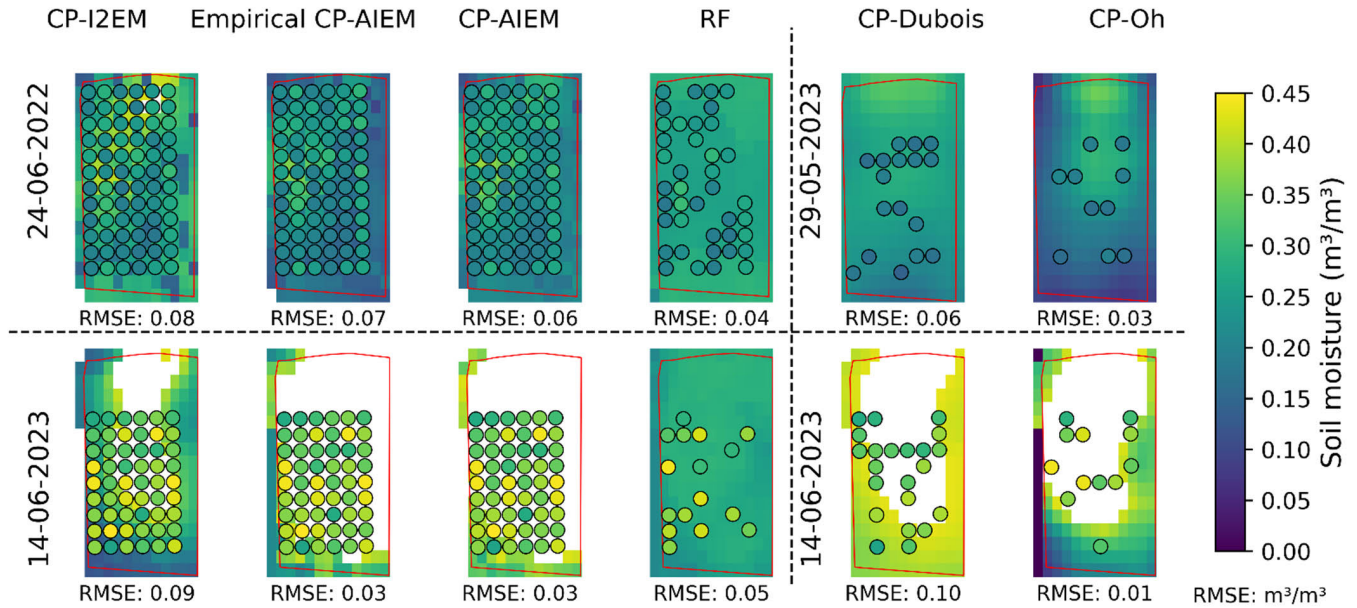
Fig. 6. Columns 1–4: Comparison of soil moisture maps generated from CP-I^{2}EM, empirical CP-AIEM, CP-AIEM, and the RF model for field B12 of AAFC-Lennoxville site for two dates of different RCM incidence angle 24-06-2022 ($\theta < 24°$) and 14-06-2023 ($\theta > 36°$). The missing values in certain fields correspond to values more than 0.45 m^3/m^3. Columns 5 and 6: Comparison of soil moisture maps generated from CP-Dubois and CP-Oh models for same field for dates 29-05-2023 and 14-06-2023. These models are not valid under lower incidence angle SAR observation. RMSE values (m^3/m^3) are mentioned below each map.

We have selected $\sigma_{CV}^0, \sigma_{CH}^0, \theta$, anisotropy ($A$), entropy ($H$), and soil texture coefficient (β) [5], ks and kl as the features for soil moisture prediction as shown in Fig. 5(a). Other parameters, such as σ_{CX}^0, α_s, surface scattering component of various CP decompositions, and degree of polarization, have not shown good correlation with FSM. The hyperparameters are tuned via grid search to maximize accuracy by minimizing cross-validation and test MSE. Cross-validation reflects the model's performance across different subsets, ensuring the training data are representative and help to avoid overfitting. The distribution of points along the reference line in the quantile-quantile (Q-Q) plot indicates that the residual of the model follows normal distribution [Fig. 5(b)]. The training (left) and testing (right) residuals are randomly scattered around zero, which indicates that the model's predictions are unbiased [Fig. 5(c)].

C. Model Inversion for Bare Soil Moisture Retrieval

The results of the retrieved soil moisture from each CP model are presented and discussed here. Fig. 6 illustrates soil moisture maps generated by each algorithm for one representative field B12 with respective RMSEs. The dates 24-06-2022 ($\theta < 30°$, dry soil) and 14-06-2023 ($\theta > 30°$, wet soil) are shown for CP-I^{2}EM, empirical CP-AIEM, CP-AIEM, and RF model approaches. Since CP-Dubois and CP-Oh models do not work at $\theta < 30°$, data of 29-05-2023 (dry soil) is displayed instead of 24-06-2022. The white areas within B12 represent noninvertible pixels for each respective retrieval. The validation samples of FSM are superimposed over the retrieved soil moisture. Under saturated soil conditions and high incidence angle (see fields on 14-06-2023), theoretical models and CP-Dubois models predict very high soil moisture values around 0.4–0.45 m^3/m^3, while CP-Oh predicts

0.3–0.4 m^3/m^3 with many noninvertible pixels (white areas in Fig. 6). The RF model also predicts 0.3–0.4 m^3/m^3. Visual comparison suggests that on this date, CP-I^{2}EM has the maximum number of inverted points (= 20), while CP-AIEM and empirical CP-AIEM have better RMSE (0.03), considering only the inverted pixels of this field. On 24-06-2022, CP-AIEM and empirical CP-AIEM have very good agreement with FSM (0.25–0.35 m^3/m^3), while CP-I^{2}EM slightly overestimates at certain locations with a few noninvertible pixels. The RF model results are also well represented for FSM. On 29-05-2023, CP-Dubois has a higher number of inverted pixels (17 versus 10), but a higher RMSE (0.06 versus 0.03) as compared to CP-Oh. The abrupt change in characteristics of the boundary pixels visible in the maps is due to the masking of images with field polygons.

Scatterplots indicating the correlation of soil moisture retrievals with FSM are presented for each CP model inversion in Fig. 7, 0 according to the incidence angle variation. Fig. 7(a) illustrates the correlation of the soil moisture retrieved from the CP-AIEM algorithm with respect to in situ FSM. Out of the total of 438 validation samples, 327 were inverted with RMSE = 0.07 m^3/m^3 with spatial IR of 64%. The retrieved soil moisture has a good correlation ($r = 0.6$, $p < 0.01$) with FSM. At $\theta > 36°$, soil moisture under dry conditions is underestimated by the model. Deeper analysis reveals that these samples correspond to fields of low kl value. The model also has a limitation to invert saturated moisture conditions ($0.4 < $ FSM < 0.45 m^3/m^3) observed on several fields due to heavy rain. Next, the soil moisture retrieval from CP-I^{2}EM with respect to the in situ FSM is displayed in Fig. 7(b). Invertible samples are 339 out of 438 total validation samples with model RMSE = 0.09 m^3/m^3. This model produces 271 samples with RMSE < 0.05 m^3/m^3 at a spatial IR of 62%. This means that there are only a few predictions which are outside
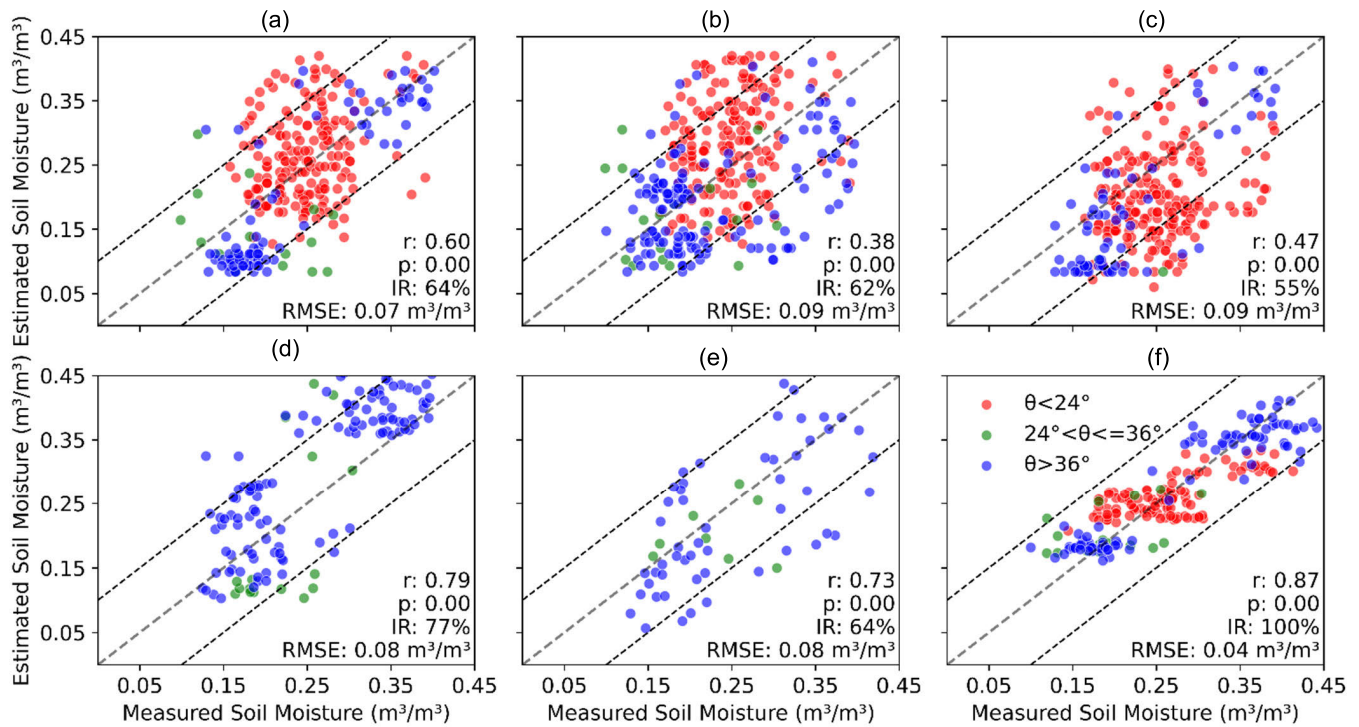
Fig. 7. Estimated soil moisture versus measured soil moisture for all 6 models (a) CP-AIEM, (b) CP-I²EM, (c) empirical CP-AIEM, (d) CP-Dubois model, (e) CP-Oh model, and (f) RF model with indication of different incidence angle cases. The statistical measures r, p, RMSE (m³/m³), and IR (%) correspond to each model are indicated.

the limit of RMSE < 0.05 m³/m³. This spatial IR value is better than the empirical CP-AIEM but inferior to CP-AIEM. There is a reduction in the number of invertible points at $\theta < 24°$, but there is are higher number of points inverted for $\theta > 36°$ under dry soil conditions. It is also worth noting that there is an accumulation of points above the 1:1 line at dry conditions due to the slight overestimation of simulated σ_{CH}^0 visible in Fig. 4. Soil moisture retrieval from the empirical CP-AIEM with respect to in situ FSM is shown in Fig. 7(c). Out of the 438 points, 311 validation samples are invertible. The model RMSE is 0.09 m³/m³. The IR here is 55% with 258 points having RMSE < 0.05 m³/m³. This is due to the overestimation of the simulated σ_{CH}^0 that was identified in Fig. 4. It also results in an accumulation of estimated soil moisture below the 1:1 line. In both empirical CP-AIEM and CP-I²EM, there are more inverted pixels than in CP-AIEM, which are out of the limit of RMSE < 0.05 m³/m³. The r, RMSE, and IR values suggest that among the three IEM-derived theoretical models, CP-AIEM performs best. Fig. 7(d) provides a correlation of estimated soil moisture from the developed CP-Dubois model with FSM. Out of 135 validation samples, 117 samples are inverted with RMSE = 0.08 m³/m³. The model performs well with 103 validation points with an RMSE < 0.05 m³/m³ (IR = 77%) without any significant bias to any of the soil conditions. A good correlation (r = 0.79, p < 0.01) is achieved between the inverted soil moisture and FSM.

In the case of soil moisture retrieval from the CP-Oh model [see Fig. 7(e)], 56 of the 67 validation samples are invertible with an RMSE = 0.08 m³/m³ and r = 0.73 (p < 0.01). In total, 43 samples have an RMSE < 0.05 m³/m³, achieving IR = 64% which is lower than for the CP-Dubois model.

The RF model approach provides soil moisture estimates of very good correlation (r = 0.88, p < 0.01) with regard to FSM [see Fig. 7(f)]. All 175 testing samples are inverted with an RMSE of 0.04 m³/m³. This result outperforms the other theoretical and empirical models. Since all the testing samples are inverted within RMSE < 0.05 m³/m³, the spatial IR is 100% in the case of the RF model. However, it must be stated immediately that the machine learning algorithm was trained under the same environmental conditions and the same fields, as it was applied subsequently. It is important to note that training and testing areas were different in the respective fields.

D. Comparison of Models

Table V quantitatively compares theoretical, empirical, and machine learning algorithms for CP-based bare soil moisture retrieval. IEM-based theoretical and RF models have validity over the whole range of the respective RCM incidence angles. CP-Dubois and CP-Oh models have a more restricted incidence angle range of 30°–43°, while the original Oh model works in a wider range. In situ ks, kl, and FSM are required for calibration and/or training of CP-Dubois, CP-Oh, and RF models (column 3). The number of validation samples available for each model is different due to the difference in validity range and calibration strategy (column 4). The number of inverted samples in each model depends on the model's capability to invert the CP backscatter to the valid range of soil moisture (0.01 < FSM < 0.45 m³/m³) (column 5). RMSE and r of each model calculated from the inverted samples is given in columns 6 and 7. RF model has the highest RMSE and

TABLE V
STATISTICAL COMPARISON OF SOIL MOISTURE INVERSION FROM THE RCM CP DATA USING THE CP-MODELS; NA = NOT APPLICABLE

Model name	RCM θ validity range	Training/ calibration samples	Validation samples	Inverted samples	RMSE (m^3/m^3)	r, $(p<0.01)$	No. of samples with RMSE < 0.05 m^3/m^3	Inversion rate for RMSE < 0.05 m^3/m^3
Empirical CPAIEM	20°-43°	NA	438	311	0.09	0.47	258	55%
CPAIEM	20°-43°	NA	438	331	0.07	0.60	291	64%
CP-I²EM	20°-43°	NA	438	345	0.09	0.38	271	62%
CP-Dubois Model	30°-43°	134	135	117	0.08	0.79	103	77%
CP-Oh Model	30°-43°	201	67	56	0.08	0.73	43	64%
RF Model	20°-43°	263	175	175	0.04	0.88	175	100%

r values (0.04 and 0.88), and empirical CP-AIEM (0.09, 0.47) and CP-I²EM (0.09, 0.38) have the lowest. CP-AIEM has the highest number of inverted points with RMSE < 0.05 m³/m³ (column 8). The IR value is highest for the RF model (100%) and lowest for empirical CP-AIEM (55%) (column 7). CP-AIEM works best among the theoretical models with the highest IR value (64%). From the quantitative comparison of the models, the RF model produces the soil moisture retrieval of the highest accuracy with sufficient training. CP-Dubois performs better than the CP-Oh model even though both have a restricted validity range. Theoretical models produce comparable soil moisture predictions without any training. Among the theoretical models, CP-AIEM has the highest agreement with FSM in most cases.

E. Discussions

In this study, we investigated the potential of C-band CP SAR observations to estimate soil moisture for bare soil under different surface roughness and incidence angle conditions. The dependence of CP backscatter on roughness parameters demonstrates their essential inclusion in the scattering model. Although CP backscatter is influenced by surface roughness, many existing soil moisture retrieval algorithms either estimate its impact using radar data [15], [46] or use parameters that are independent of roughness [14]. We acknowledge this influence and use the in situ measurements of roughness to maintain our focus on accurate soil moisture estimation. Our findings suggest that the previously reported consideration of roughness independence on polarimetric scattering angle (α_s) [14] may not fully apply to the specific bare soil conditions and C-band SAR in our study. The developed theoretical models (empirical CP-AIEM, CP-AIEM, and CP-I²EM) are simulated and tested at various soil moisture, surface roughness, texture, and incidence angle conditions. We observed that simulated CP backscatters show similarities with the simulated FP co-polarization backscatters [26], [28] at various surface and observation geometries. Similar to the comparative analysis presented in [37] our evaluation using real in situ data reveals the applicability of each model under varying field conditions. CP-AIEM soil moisture estimates have comparable RMSE (0.07 versus 0.06 m³/m³ in [14]) under similar conditions, while our study area encompasses a wide

range of FSM conditions. Usage of the analytical relationship between FP and CP backscatter emphasizes the reliability of CP-AIEM and CP-I²EM instead of using an empirical equation [15]. The RMSE of soil moisture retrieval from our models (0.07–0.09 m³/m³) are better at different roughness conditions as compared to [15] with RMSE 0.11 m³/m³. The CP-Dubois model predicts soil moisture with accuracy inferior to the original Dubois model for C-band [48] which indicates the requirement of improving the model calibration for CP backscatter. Previous adaptations of the Oh model for FP [46] reported consistent performances across incidence angles, whereas our CP-Oh model demonstrates optimal accuracy only at higher incidence angles (>30°). This suggests that the CP-based calibration of empirical models needs to be further investigated with larger datasets. Nonetheless, the performance of CP-Dubois and CP-Oh models in this study is reliable and encouraging. The constants are calibrated with our unique on-site training data for agricultural land use, which is characterized by a very high variability in terms of study sites, soil moisture, roughness, and incidence angle. Finally, the RF model provides comparable soil moisture retrieval accuracy as that of previously developed and tested machine-deep learning methods with RMSE < 0.04 m³/m³ [18], [49]. Increasing the testing-training split from 40:60 to 25:75 would effectively improve the performance of the RF model as well. However, in this work, we limit our focus to the development of theoretical and empirical models.

VI. CONCLUSION AND OUTLOOK

The main contribution and novelty of this article is the development of theoretical (empirical CP-AIEM, CP-AIEM, and CP-I²EM) and empirical (CP-Dubois model, CP-Oh model) CP backscattering models for bare soil moisture retrievals. Machine learning is used here for comparison purposes only and is not considered a targeted contribution. It can be concluded that the usage of physical relationships between FP and CP scattering matrices is the key advantage of CP-AIEM and CP-I²EM over empirical CP-AIEM, in which the empirical relationships between FP and CP backscattering coefficients are used. The developed theoretical models are valid for the entire incidence angle and roughness range considered in this work. The recalibrated empirical models are valid only at higher incidence angles ($\theta > 30°$). CP-AIEM

demonstrates better capability among the theoretical models with the highest r, IR, and lowest RMSE. The CP-Dubois performs better than the CP-Oh model among the empirical models. With sufficient training, the RF model provides better accuracy than the other models. It is indicated by our results that CP-AIEM will be the best choice for soil moisture retrievals among the six proposed models, considering its accuracy and validity range without requiring a calibration step. The main advantage is the ability to interpret the results. However, further work is needed to improve accuracy in comparison to the machine learning RF model.

A key limitation of this study is the roughness measurement, which is restricted only to two locations of each field at the beginning of the season and texture parameters are measured only once per season at a single location in each field. This shortcoming may inadequately capture spatial and temporal variability. Nevertheless, having field-specific measurements on not only soil moisture but also soil roughness, rather than generalized parameters (from literature), significantly strengthens our model. It enhances the overall robustness in developing and testing our soil moisture retrievals.

In the future, more samples collected under various surface and acquisition geometry conditions will help to optimally calibrate and validate the developed empirical models. Moreover, the improvement and applicability of the proposed surface scattering models for CP soil moisture retrievals must also be investigated in future studies under vegetated conditions. This work focused only on bare soil conditions and C-band CP data of RCM. Hence, the proposed models need to be validated with multifrequency datasets in future studies.

ACKNOWLEDGMENT

REFERENCES

[1] A. K. Fung, Z. Li, and K. S. Chen, "Backscattering from a randomly rough dielectric surface," *IEEE Trans. Geosci. Remote Sens.*, vol. 30, no. 2, pp. 356–369, Mar. 1992, doi: 10.1109/36.134085.

[2] J. Shang, J. Liu, Z. Chen, H. Mcnairn, and A. Davidson. (2022). *Recent Advancement of Synthetic Aperture Radar (SAR) Systems and Their Applications to Crop Growth Monitoring*. [Online]. Available: http://www.intechopen.com

[3] P. C. Dubois and J. Van Zyl, "An empirical soil moisture estimation algorithm using imaging radar," in *Proc. IEEE Int. Geosci. Remote Sens. Symp.*, vol. 3, Aug. 1994, pp. 1573–1575, doi: 10.1109/IGARSS.1994.399501.

[4] K. S. Chen, *Radar Scattering and Imaging of Rough Surfaces*, vol. 1, 1st ed., Boca Raton, FL, USA: CRC Press, 2021.

[5] M. Dobson, F. Ulaby, M. Hallikainen, and M. El-rayes, "Microwave dielectric behavior of wet soil-part II: Dielectric mixing models," *IEEE Trans. Geosci. Remote Sens.*, vols. GE-23, no. 1, pp. 35–46, Jan. 1985, doi: 10.1109/TGRS.1985.289498.

[6] V. L. Mironov, M. C. Dobson, V. H. Kaupp, S. A. Komarov, and V. N. Kleshchenko, "Generalized refractive mixing dielectric model for moist soils," *IEEE Trans. Geosci. Remote Sens.*, vol. 42, no. 4, pp. 773–785, Apr. 2004, doi: 10.1109/TGRS.2003.823288.

[7] M. Hallikainen, F. Ulaby, M. Dobson, M. El-rayes, and L.-K. Wu, "Microwave dielectric behavior of wet soil-part 1: Empirical models and experimental observations," *IEEE Trans. Geosci. Remote Sens.*, vols. GE-23, no. 1, pp. 25–34, Jan. 1985, doi: 10.1109/TGRS.1985.289497.

[8] F. T. Ulaby and D. Long, "Surface-scattering models and land observations," in *Microwave Radar and Radiometric Remote Sensing*. Ann Arbor, MI, USA: The Univ. of Michigan Press, 2015, pp. 420–459. [Online]. Available: http://ebookcentral.proquest.com/lib/usherbrookemgh-ebooks/detail.action?docID=4537961

[9] F. J. Charbonneau et al., "Compact polarimetry overview and applications assessment," *Can. J. Remote Sens.*, vol. 36, no. sup2, pp. S298–S310, Jan. 2010. [Online]. Available: http://pubservices.nrc-cnrc.ca/cjrs

[10] R. K. Raney, "Hybrid-polarity SAR architecture," *IEEE Trans. Geosci. Remote Sens.*, vol. 45, no. 11, pp. 3397–3404, Nov. 2007, doi: 10.1109/TGRS.2007.895883.

[11] A. Babu, S. Kumar, and S. Agrawal, "Polarimetric calibration of RISAT-1 compact-pol data," *IEEE J. Sel. Topics Appl. Earth Observ. Remote Sens.*, vol. 12, no. 10, pp. 3731–3736, Oct. 2019, doi: 10.1109/JSTARS.2019.2932019.

[12] A. Vashishtha and S. Kumar, "Characterization of geomorphological features of lunar surface using Chandrayaan-1 mini-SAR and LRO mini-RF data," *Quaternary Int.*, vols. 575–576, pp. 338–357, Feb. 2021, doi: 10.1016/j.quaint.2020.08.018.

[13] R. K. Raney, B. Brisco, M. Dabboor, and M. Mahdianpari, "RADARSAT constellation mission's operational polarimetric modes: A user-driven radar architecture," *Can. J. Remote Sens.*, vol. 47, no. 1, pp. 1–16, 2021, doi: 10.1080/07038992.2021.1907566.

[14] G. G. Ponnurangam, T. Jagdhuber, I. Hajnsek, and Y. S. Rao, "Soil moisture estimation using hybrid polarimetric SAR data of RISAT-1," *IEEE Trans. Geosci. Remote Sens.*, vol. 54, no. 4, pp. 2033–2049, Apr. 2016, doi: 10.1109/TGRS.2015.2494860.

[15] A. Merzouki, H. McNairn, J. Powers, and M. Friesen, "Synthetic aperture radar (SAR) compact polarimetry for soil moisture retrieval," *Remote Sens.*, vol. 11, no. 19, p. 2227, Sep. 2019, doi: 10.3390/rs11192227.

[16] I. Zakharov, S. Kohlsmith, J. Hornung, F. Charbonneau, P. Bobby, and M. Howell, "Surface soil moisture estimation from time series of RADARSAT constellation mission compact polarimetric data for the identification of water-saturated areas," *Remote Sens.*, vol. 16, no. 14, p. 2664, Jul. 2024, doi: 10.3390/rs16142664.

[17] M. Dabboor et al., "The RADARSAT constellation mission for soil moisture retrieval of bare soil by compact polarimetry and random forest regression," *Can. J. Remote Sens.*, vol. 50, no. 1, pp. 1–19, Dec. 2024, doi: 10.1080/07038992.2024.2356688.

[18] X. Zhou and J. Wang, "Soil moisture retrieval over crop region using time-series high-resolution RCM data," in *Proc. IEEE Int. Geosci. Remote Sens. Symp.*, Jul. 2023, pp. 3578–3581, doi: 10.1109/IGARSS52108.2023.10281694.

[19] *The TanDEM-X 30m Edited Digital Elevation Model (EDEM) and DEM Change Maps (DCM)*, German Aerospace Center, Cologne, Germany.

[20] R. Touzi, M. Lapointe, M. A. Fobert, S. Nedelcu, and S. Côté, "Assessment and calibration of RCM compact-hybrid modes," in *Proc. IEEE Int. Geosci. Remote Sens. Symp.*, Jul. 2023, pp. 7840–7843.

[21] S. Allain, "Caractérisation d'un sol nu á partir de données SAR polarimétriques Etude multi-fréquentielle et multi-résolutions," Université Rennes, Rennes, France, Tech. Rep., 2003.

[22] (2017). *User Manual for the Moisture Meter Type HH2*. [Online]. Available: http://www.delta-t.co.uk

[23] M. Trudel, F. Charbonneau, F. Avendano, and R. Leconte, "Quick profiler (QuiP): A friendly tool to extract roughness statistical parameters using a needle profiler," *Can. J. Remote Sens.*, vol. 36, no. 4, pp. 391–396, Jan. 2010, doi: 10.5589/m10-070.

[24] P. Hermansson, G. Forssell, and J. Fagerström, "Sensor technology SE-581 11 LinköPing a review of models for scattering from rough surfaces," Swedish Defence Res. Agency, Kista, Sweden, Tech. Rep., 2003.

[25] J. L. Álvarez-Pérez, "An extension of the IEM/IEMM surface scattering model," *Waves Random Media*, vol. 11, no. 3, pp. 307–329, Jul. 2001. [Online]. Available: http://www.iop.org/Journals/wr

[26] A. K. Fung, W. Y. Liu, K. S. Chen, and M. K. Tsay, "An improved iem model for bistatic scattering from rough surfaces," *J. Electromagn. Waves Appl.*, vol. 16, no. 5, pp. 689–702, Jan. 2002, doi: 10.1163/156939302x01119.

[27] K. S. Chen, T.-D. Wu, L. Tsang, Q. Li, J. Shi, and A. K. Fung, "Emission of rough surfaces calculated by the integral equation method with comparison to three-dimensional moment method simulations," *IEEE Trans. Geosci. Remote Sens.*, vol. 41, no. 1, pp. 90–101, Jan. 2003, doi: 10.1109/TGRS.2002.807587.

[28] T.-D. Wu and K.-S. Chen, "A reappraisal of the validity of the IEM model for backscattering from rough surfaces," *IEEE Trans. Geosci. Remote Sens.*, vol. 42, no. 4, pp. 743–753, Apr. 2004, doi: 10.1109/TGRS.2003.815405.

[29] N. Baghdadi, K. Cock, N. Baghdadi, C. King, A. Chanzy, and J. P. Wigneron, "An empirical calibration of IEM model based on SAR data and measurements of soil moisture and surface roughness over bare soils," *Article Int. J. Remote Sens.*, vol. 23, no. 20, pp. 4325–4340, 2002. [Online]. Available: https://www.researchgate.net/publication/236882077

[30] N. Baghdadi, I. Gherboudj, M. Zribi, M. Sahebi, C. King, and F. Bonn, "Semi-empirical calibration of the IEM backscattering model using radar images and moisture and roughness field measurements," *Int. J. Remote Sens.*, vol. 25, no. 18, pp. 3593–3623, Sep. 2004, doi: 10.1080/01431160310001654392.

[31] N. Baghdadi, N. Holah, and M. Zribi, "Calibration of the integral equation model for SAR data in C-band and HH and VV polarizations," *Int. J. Remote Sens.*, vol. 27, no. 4, pp. 805–816, Feb. 2006, doi: 10.1080/01431160500212278.

[32] J. Yang, Y. Li, J. C. Shi, and Y. Du, "Modification of the extended advanced IEM for scattering from randomly rough surfaces," *IEEE Geosci. Remote Sens. Lett.*, vol. 18, no. 2, pp. 236–240, Feb. 2021, doi: 10.1109/LGRS.2020.2971532.

[33] L. De Laurentiis, D. Latini, G. Schiavon, and F. Del Frate, "Integration of IEM_B, ISMN and SAR Sentinel-1 data for accurate soil moisture estimation using neural networks," in *Proc. IEEE Int. Geosci. Remote Sens. Symp. IGARSS*, Jul. 2021, pp. 1272–1275, doi: 10.1109/IGARSS47720.2021.9554701.

[34] H.-J.-F. Benninga, R. van der Velde, and Z. Su, "Soil moisture content retrieval over meadows from Sentinel-1 and Sentinel-2 data using physically based scattering models," *Remote Sens. Environ.*, vol. 280, Oct. 2022, Art. no. 113191, doi: 10.1016/j.rse.2022.113191.

[35] Y. Oh, K. Sarabandi, and F. T. Ulaby, "An empirical model and an inversion technique for radar scattering from bare soil surfaces," *IEEE Trans. Geosci. Remote Sens.*, vol. 30, no. 2, pp. 370–981, Mar. 1992.

[36] P. C. Dubois, J. vanZyl, and T. Engman, "Corrections to 'Measuring soil moisture with imaging radars,'" *IEEE Trans. Geosci. Remote Sens.*, vol. GRS-33, no. 6, p. 1340, Nov. 1995.

[37] M. Choker et al., "Evaluation of the oh, Dubois and IEM backscatter models using a large dataset of SAR data and experimental soil measurements," *Water*, vol. 9, no. 1, p. 38, Jan. 2017, doi: 10.3390/w9010038.

[38] S. Roy et al.. (2024). *Integration of Modified Water Cloud and Dubois Models With Novel Interaction Terms for Precise Estimation of Soil Moisture and Leaf Area Index From C-Band SAR Data*. [Online]. Available: https://ssrn.com/abstract=4963946

[39] M. Sadeghi, S. Karimzadeh, and K. Valizadeh Kamran. (2024). *Surface Soil Moisture Retrieval Using Sentinel-1 SAR Data Models Dubois in Ardabil Plain*. [Online]. Available: https://www.researchgate.net/publication/383035053

[40] W. Han et al., "Spatial series approach to estimate soil moisture over wheat fields from a single SAR image," *Agricult. Water Manage.*, vol. 321, Dec. 2025, Art. no. 109883, doi: 10.1016/j.agwat.2025.109883.

[41] S. Najem, N. Baghdadi, H. Bazzi, M. Zribi, D. K. Pandey, and M. Sekhar, "Bare surface soil moisture and surface roughness estimation using multi-band multi-polarization NISAR-like SAR data," *Frontiers Remote Sens.*, vol. 6, pp. 1–17, Jul. 2025, doi: 10.3389/frsen.2025.1613748.

[42] P. Settu and M. Ramaiah, "Estimation of Sentinel-1 derived soil moisture using modified Dubois model," *Environ., Develop. Sustainability*, vol. 26, no. 11, pp. 29677–29693, Oct. 2024, doi: 10.1007/s10668-024-05460-1.

[43] Z. Dong, M. Gao, and A. Karnieli, "Soil moisture retrieval in the northeast China Plain's agricultural fields using single-temporal L-band SAR and the coupled MWCM-oh model," *Remote Sens.*, vol. 17, no. 3, p. 478, Jan. 2025, doi: 10.3390/rs17030478.

[44] L. Li et al., "Enhancing deep learning soil moisture forecasting models by integrating physics-based models," *Adv. Atmos. Sci.*, vol. 41, no. 7, pp. 1326–1341, Jul. 2024, doi: 10.1007/s00376-023-3181-8.

[45] A. Muhuri, K. Goïta, R. Magagi, and H. Wang, "Soil moisture retrieval during crop growth cycle using satellite SAR time series," *IEEE J. Sel. Topics Appl. Earth Observ. Remote Sens.*, vol. 16, pp. 9302–9319, 2023, doi: 10.1109/JSTARS.2023.3280181.

[46] H. Wang, S. Méric, S. Allain, and É. Pottier, "Adaptation of oh model for soil parameters retrieval using multi-angular RADARSAT-2 datasets," *J. Surveying Mapping Eng.*, vol. 2, no. 4, pp. 1–10, 2014. [Online]. Available: https://hal.science/hal-01127973

[47] Y. Oh, "Quantitative retrieval of soil moisture content and surface roughness from multipolarized radar observations of bare soil surfaces," *IEEE Trans. Geosci. Remote Sens.*, vol. 42, no. 3, pp. 596–601, Mar. 2004, doi: 10.1109/TGRS.2003.821065.

[48] R. Dave, G. Kumar, D. Kr. Pandey, A. Khan, and B. Bhattacharya, "Evaluation of modified Dubois model for estimating surface soil moisture using dual polarization RISAT-1 C-band SAR data," *Geocarto Int.*, vol. 36, no. 13, pp. 1459–1469, Aug. 2021, doi: 10.1080/10106049.2019.1655801.

[49] M. Dabboor, G. Atteia, S. Meshoul, and W. Alayed, "Deep learning-based framework for soil moisture content retrieval of bare soil from satellite data," *Remote Sens.*, vol. 15, no. 7, p. 1916, Apr. 2023, doi: 10.3390/rs15071916.

[50] E. Santi, M. Dabboor, S. Pettinato, and S. Paloscia, "Combining machine learning and compact polarimetry for estimating soil moisture from C-band SAR data," *Remote Sens.*, vol. 11, no. 20, p. 2451, Oct. 2019, doi: 10.3390/rs11202451.

[51] F. Greifeneder, C. Notarnicola, and W. Wagner, "A machine learning-based approach for surface soil moisture estimations with Google Earth engine," *Remote Sens.*, vol. 13, no. 11, p. 2099, May 2021, doi: 10.3390/rs13112099.

[52] H. Acar, M. S. Ozerdem, and E. Acar, "Soil moisture inversion via semiempirical and machine learning methods with full-polarization RadarSAT-2 and polarimetric target decomposition data: A comparative study," *IEEE Access*, vol. 8, pp. 197896–197907, 2020, doi: 10.1109/ACCESS.2020.3035235.

[53] M. Belgiu and L. Drăguţ, "Random forest in remote sensing: A review of applications and future directions," *ISPRS J. Photogramm. Remote Sens.*, vol. 114, pp. 24–31, Apr. 2016, doi: 10.1016/j.isprsjprs.2016.01.011.

[54] R. K. Raney, "Polarimetric portraits," *Earth Space Sci.*, vol. 8, no. 7, pp. 1–10, Jul. 2021, doi: 10.1029/2021ea001768.

[55] V. Kumar, D. Mandal, A. Bhattacharya, and Y. S. Rao, "Crop characterization using an improved scattering power decomposition technique for compact polarimetric SAR data," *Int. J. Appl. Earth Observ. Geoinf.*, vol. 88, Jun. 2020, Art. no. 102052, doi: 10.1016/j.jag.2020.102052.

[56] R. K. Raney, "Hybrid dual-polarization synthetic aperture radar," *Remote Sens.*, vol. 11, no. 13, p. 1521, Jun. 2019, doi: 10.3390/rs11131521.

[57] S. R. Cloude, D. G. Goodenough, and H. Chen, "Compact decomposition theory," *IEEE Geosci. Remote Sens. Lett.*, vol. 9, no. 1, pp. 28–32, Jan. 2012, doi: 10.1109/LGRS.2011.2158983.

[58] M. A. Amirabadi, M. H. Kahaei, and S. A. Nezamalhosseini, "Active learning for OPM in FMF systems," *Phys. Commun.*, vol. 58, Jun. 2023, Art. no. 102042, doi: 10.1016/j.phycom.2023.102042.

[59] C. Carranza, C. Nolet, M. Pezij, and M. van der Ploeg, "Root zone soil moisture estimation with random forest," *J. Hydrol.*, vol. 593, Feb. 2021, Art. no. 125840, doi: 10.1016/j.jhydrol.2020.125840.

[60] S. Datta, P. Das, D. Dutta, and R. K. Giri, "Estimation of surface moisture content using Sentinel-1 C-band SAR data through machine learning models," *J. Indian Soc. Remote Sens.*, vol. 49, no. 4, pp. 887–896, Apr. 2021, doi: 10.1007/s12524-020-01261-x.

[61] X. Li, F. Chadwick, and B. Swallow, "Advances in approximate Bayesian inference for models in epidemiology," *Epidemics*, vol. 53, Dec. 2025, Art. no. 100855, doi: 10.1016/j.epidem.2025.100855.

[62] Y. Shi and R. Eberhart, "A modified particle swarm optimizer," in *Proc. IEEE Int. Conf. Evol. Comput.*, May 1998, pp. 69–73.

[63] L. Cicci, S. Fresca, and A. Manzoni, "Deep-HyROMnet: A deep learning-based operator approximation for hyper-reduction of nonlinear parametrized PDEs," *J. Sci. Comput.*, vol. 93, no. 2, pp. 1–37, Nov. 2022, doi: 10.1007/s10915-022-02001-8.

[64] C. Ma, X. Li, C. Notarnicola, S. Wang, and W. Wang, "Uncertainty quantification of soil moisture estimations based on a Bayesian probabilistic inversion," *IEEE Trans. Geosci. Remote Sens.*, vol. 55, no. 6, pp. 3194–3207, Jun. 2017, doi: 10.1109/TGRS.2017.2664078.

[65] X. Li, F. Chadwick, and B. Swallow, "Advances in approximate Bayesian inference for models in epidemiology," *Epidemics*, vol. 53, Dec. 2025, doi: 10.1016/j.epidem.2025.100855.

[66] K. C. Kornelsen and P. Coulibaly, "Advances in soil moisture retrieval from synthetic aperture radar and hydrological applications," *J. Hydrol.*, vol. 476, pp. 460–489, Jan. 2013, doi: 10.1016/j.jhydrol.2012.10.044.